UNIVERSITY OF LEEDS

This is a repository copy of *High-pressure, temperature elasticity of Fe- and Al-bearing MgSiO3: implications for the Earth's lower mantle*.

White Rose Research Online URL for this paper:
http://eprints.whiterose.ac.uk/92113/

Version: Supplemental Material

Article:

Zhang, S, Cottaar, S, Liu, T et al. (2 more authors) (2016) High-pressure, temperature elasticity of Fe- and Al-bearing MgSiO3: implications for the Earth's lower mantle. Earth and Planetary Science Letters, 434. pp. 264-273. ISSN 0012-821X

https://doi.org/10.1016/j.epsl.2015.11.030

© 2015, Elsevier. Licensed under the Creative Commons Attribution-NonCommercial-NoDerivatives 4.0 International
http://creativecommons.org/licenses/by-nc-nd/4.0/

Reuse
Unless indicated otherwise, fulltext items are protected by copyright with all rights reserved. The copyright exception in section 29 of the Copyright, Designs and Patents Act 1988 allows the making of a single copy solely for the purpose of non-commercial research or private study within the limits of fair dealing. The publisher or other rights-holder may allow further reproduction and re-use of this version - refer to the White Rose Research Online record for this item. Where records identify the publisher as the copyright holder, users can verify any specific terms of use on the publisher's website.

Takedown
If you consider content in White Rose Research Online to be in breach of UK law, please notify us by emailing eprints@whiterose.ac.uk including the URL of the record and the reason for the withdrawal request.

White Rose
university consortium
Universities of Leeds, Sheffield & York

eprints@whiterose.ac.uk
https://eprints.whiterose.ac.uk/

High- pressure, temperature elasticity of Fe- and Al-bearing $MgSiO_3$: implications for the Earth's lower mantle [Supplementary Material]

Shuai Zhang[a], Sanne Cottaar[b] , Tao Liu[c], Stephen Stackhouse[c], Burkhard Militzer[a,d]

[a]*Department of Earth and Planetary Science,*
University of California, Berkeley, California 94720, USA
[b]*Department of Earth Sciences, University of Cambridge, Cambridge, UK*
[c]*School of Earth and Environment, University of Leeds, Leeds LS2 9JT, UK*
[d]*Department of Astronomy, University of California, Berkeley, California 94720, USA*

1. Theory

1.1. *Energy comparison*

The Gibbs free energy of a system with fixed configuration consists of an enthalpy term *H* and an entropy term *TS*, where *S* is a sum of vibrational and magnetic contribution. For each iron, the magnetic entropy $S_{\mathrm{mag}}=k_{\mathrm{B}}\ln[m(2S+1)]$, where *m* is the degeneracy and *S* is the spin momentum number. In both A- and B-sites of the Pv and pPv structures, $S_{\mathrm{mag}} = k_{\mathrm{B}}\ln 6$ regardless of HS or LS[1]. Therefore, we don't consider the difference in magnetic entropy between different magnetic configurations. Assuming similar vibrational entropy (Tsuchiya et al., 2006), we can just compare the enthalpies to obtain stability information.

1.2. *Data quality check---supercell size*

Both the 2x2x1 supercell for Pv and 3x1x1 supercell for pPv have been used in a number of previous studies. To confirm that finite-size effects are not an issue for supercells of this size we computed, we computed elastic and seismic properties using three different pPv supercells. The results are listed in Table S1, and show excellent agreement.

Table S1

Elastic and seismic properties of $MgSiO_3$ pPv at 125 GPa and 3500 K calculated with different supercell sizes. The values in parenthesis are the error on the last digit of the corresponding values.

supercell	K^S[GPa]	G[GPa]	V_ϕ[km/s]	V_s[km/s]	V_p [km/s]
3x1x1*	645(8)	298(7)	10.95(7)	7.45(8)	13.92(8)
4x1x1#	644(9)	301(8)	10.94(8)	7.48(10)	13.94(10)
4x2x2&	644(4)	291(4)	10.95(4)	7.36(5)	13.86(5)

*: c/a=2.459, b/a=3.244, ρ=5373 kg/m^3

#: c/a =2.471, b/a =3.261, ρ=5378 kg/m^3

&: c/a =2.477, b/a =3.268, ρ=5365 kg/m^3

---

[1] For ferric iron, the spin momentum *S*(HS)=5/2 and *S*(LS)=1/2; the orbit degeneracy *m*(HS)=1 and *m*(LS)=3, regardless of A (dodecahedral) or B (octahedral) site. Therefore, the magnetic entropy $S_{\mathrm{mag}}(\mathrm{HS})= k_{\mathrm{B}}\ln[1\times(2\times5/2+1)]= k_{\mathrm{B}}\ln 6$; $S_{\mathrm{mag}}(\mathrm{LS})= k_{\mathrm{B}}\ln[3\times(2\times1/2+1)]= k_{\mathrm{B}}\ln 6$.

1.3. Data quality check---k-mesh

To test convergence with respect to *k*-point sampling we compare the elastic and seismic properties of $MgSiO_3$ pPv calculated using four different Monkhorst-Pack *k*-meshes (Monkhorst and Pack, 1976) in the NVT stage (Table S2). A separate test using a denser *k*-mesh at the NPT and Γ-point at the NVT stage is compared with the Γ-only calculations for pPv at 125 GPa and 2500K (Table S3).

Table S2

Elastic and seismic properties of $MgSiO_3$ pPv at 125 GPa and 3500 K calculated with the 3x1x1 supercell and different *k*-meshes during NVT. The values in parenthesis are the error on the last digit of the corresponding values.

k-mesh	K^S[GPa]	G[GPa]	V_ϕ[km/s]	V_s[km/s]	V_p [km/s]
Γ -only	645(8)	298(7)	10.95(7)	7.45(8)	13.92(8)
2x2x2	667(10)	284(8)	11.14(9)	7.27(10)	13.95(10)
3x3x3	626(12)	292(9)	10.79(11)	7.37(11)	13.74(12)
4x4x4	641(14)	292(11)	10.92(12)	7.37(14)	13.84(13)

Table S3

Elastic and seismic properties of $MgSiO_3$ pPv at 125 GPa and 2500 K calculated with the 3x1x1 supercell and different *k*-meshes during NPT and Γ-only during NVT. The values in parenthesis are the error on the last digit of the corresponding values.

k-mesh	K^S[GPa]	G[GPa]	V_ϕ[km/s]	V_s[km/s]	V_p [km/s]
Γ -only*	655(7)	315(5)	10.97(6)	7.61(6)	14.05(6)
2x2x2#	668(7)	318(5)	11.09(6)	7.65(6)	14.17(7)

*: c/a=2.463, b/a=3.246, ρ=5444 kg/m^3; #: c/a =2.464, b/a =3.247, ρ=5438 kg/m^3

1.4. Data quality check---DFT+U for better accounting the correlation effects

We performed DFT+U calculations for a Fe^{3+}-bearing Pv structure (fepv6) with one Fe-Fe pair taking an A (HS) and a B (LS) site, respectively, in the unit cell, at 125 GPa and 2500K. The results (Table S4) show remarkable consistency with standard LDA calculations on sound velocities and seismic properties.

Table S4

Comparison on elastic constants, bulk and shear moduli, sound velocities, and transverse isotropy at different slip planes of (Mg$_{1-x}$Fe$_x$)(Si$_{1-x}$Fe$_x$)O$_3$, x=6.25% (fepv6) at 100 GPa and 2500 K calculated by LDA and four different types of LDA+U: NVT only, both NPT and NVT (relax), same U for Fe at A and B sites, different U for Fe at A and B sites. The values in parenthesis are the error on the last digit of the corresponding values.

Fepv6, HS-LS	LDA[*]	LDA+U (U=6)	LDA+U (U1=6, U2=4.8)	LDA+U-relax[#] (U=6)	LDA+U-relax[&] (U1=6, U2=4.8)
ρ [kg/m^3]	5300	5300	5300	5300	5296
C11[GPa]	752(29)	732(38)	729(38)	689(31)	749(34)
C22[GPa]	958(37)	957(33)	955(31)	901(30)	1040(29)
C33[GPa]	894(22)	895(27)	895(27)	922(31)	842(38)
C12[GPa]	482(11)	485(11)	480(11)	507(11)	492(10)
C13[GPa]	361(10)	364(11)	363(11)	358(10)	350(11)
C23[GPa]	362(10)	366(10)	370(10)	407(10)	352(10)
C44[GPa]	268(19)	270(20)	271(19)	277(17)	282(21)
C55[GPa]	226(17)	220(13)	220(13)	221(23)	209(14)
C66[GPa]	289(24)	293(26)	287(28)	244(30)	258(24)
K[GPa]	558(10)	557(11)	557(11)	562(10)	558(11)
G[GPa]	250(8)	248(9)	247(9)	231(10)	246(9)
V_ϕ[km/s]	10.26(9)	10.26(10)	10.25(10)	10.30(10)	10.27(10)
V_s[km/s]	6.87(11)	6.84(12)	6.82(12)	6.61(14)	6.81(12)
V_p [km/s]	12.97(11)	12.95(11)	12.93(11)	12.82(12)	12.93(11)
ξ(001)	0.96(8)	0.96(8)	0.95(8)	0.78(8)	0.93(8)
ξ(100)	1.07(8)	1.07(7)	1.08(8)	1.14(11)	1.23(9)
ξ(010)	0.82(6)	0.79(7)	0.80(7)	0.85(7)	0.80(7)

*: $2c/3a$=0.968, b/a=1.055; #: $2c/3a$=0.968, b/a=1.055; &: $2c/3a$=0.968, b/a=1.054

1.5. Data quality check

The statistical average of the 6 stress components and their convergence with the length of the NVT-MD simulations are illustrated in Fig. S1. Good convergence is typically reached in 5 ps.

The elastic constants derived from different stress-strain relations are compared in Fig. S2. The consistence shows the reliability of the calculated elastic constants based on our choice of strain $\epsilon = \pm 0.5\%$ and good linearity at such small strains.

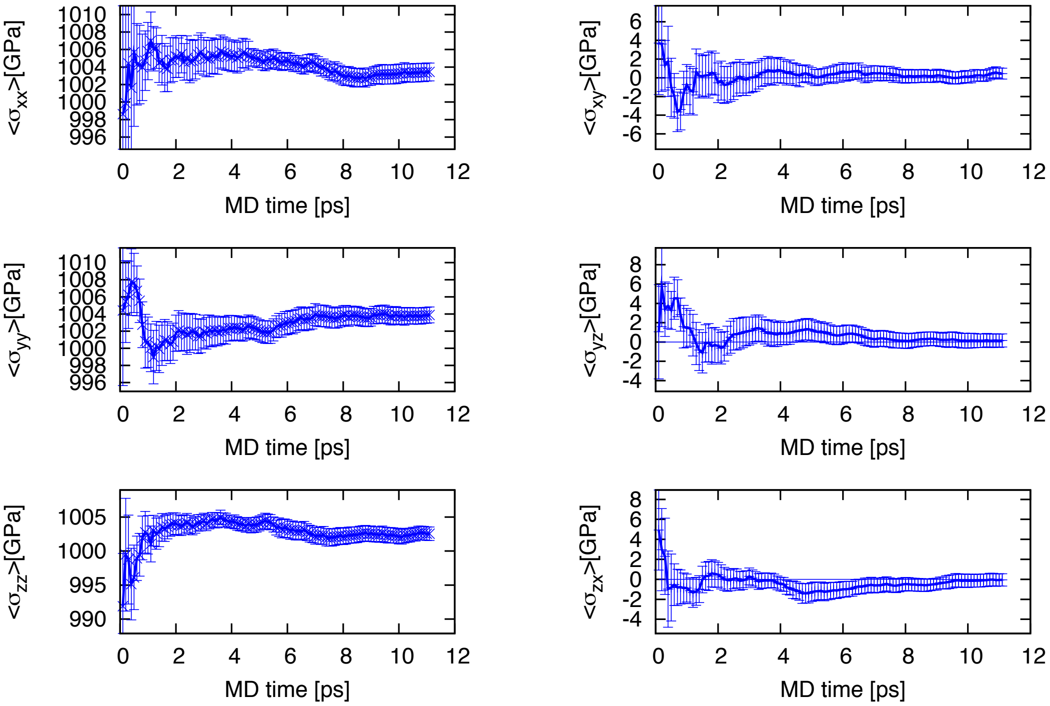

Fig. S1 (color online). The statistical average of the six stress components calculated as functions of the length of the molecular-dynamic simulations.

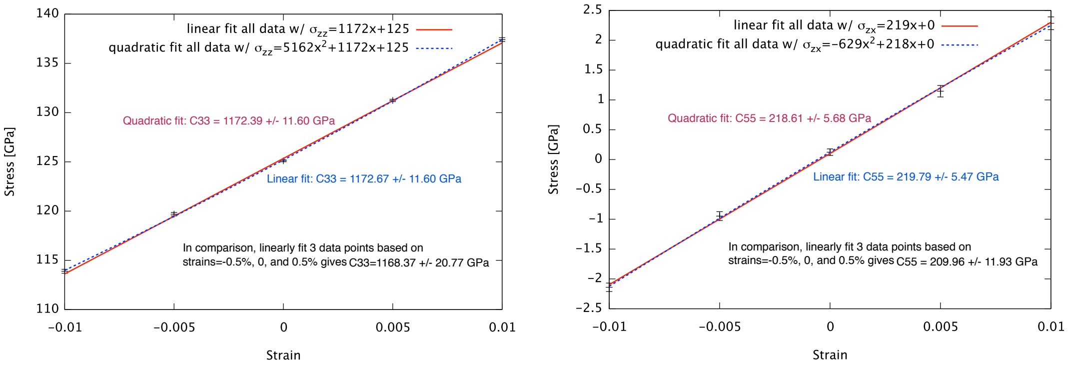

Fig. S2 (color online). Comparison on elastic constants (C_{33} on the left and C_{55} on the right, for $(Mg_{0.92}Fe_{0.08})(Si_{0.92}Al_{0.08})O_3$ at 125 GPa and 2500 K) as calculated by assuming linear or quadratic stress-strain relations. Using the small strains chosen here (0.5%), the linearity is evident.

1.6. Pressure correction

We start from the ambient-condition volume of $MgSiO_3$ perovskite from the experiments of Fiquet et al. (2000) and Shieh et al. (2006) and estimate[2] the true unit cell volume at T=0 K to be 161.8~162.8 Å^3. LDA calculations with the volume of the $MgSiO_3$ perovskite cell fixed at these values return pressures P^{LDA}=-3.5~-5.0 GPa. Therefore, we choose $\Delta P = +4.0$ GPa as a rigid shift to the calculated pressures to reconcile the methodological underestimation, and assume it is independent of mineral phases in this study. This choice is consistent with the inadequate value (1.9 GPa) suggested in Zhang et al. (2013) and similar to the finding in recent Quantum Monte Carlo calculations (Lin et al., 2014).

Table S5

Comparison between the elastic and seismic properties of different minerals calculated using the Voigt (V) and the Voigt-Reuss-Hill (VRH) scheme at 125 GPa and 2500 K. Density, moduli, and velocities are in units of kg/m³, GPa, and km/s, respectively.

		ρ	K_V^S	K_V^S-K_{VRH}	G_V	G_V-G_{VRH}	$V_{\phi,V}$	$V_{\phi,V}$-$V_{\phi,VRH}$	V_{sV}	$V_{s,V}$-$V_{s,VRH}$	$V_{p,V}$	$V_{p,V}$-$V_{p,VRH}$
Pv	$MgSiO_3$	5367	673(6)	6	288(5)	5	11.20(5)	0.05	7.32(7)	0.06	14.03(6)	0.08
$(Mg_{1-x}Fe_x)(Si_{1-x}Al_x)O_3$	x=6.25%	5451	655(7)	5	270(6)	2	10.96(6)	0.04	7.04(7)	0.03	13.65(7)	0.06
$(Mg_{1-x}Fe_x)(Si_{1-x}Fe_x)O_3$	x=6.25%	5541	664(7)	4	285(6)	4	10.95(6)	0.04	7.17(7)	0.05	13.72(7)	0.06
$(Mg_{1-x}Fe_x)(Si_{1-x}Al_x)O_3$	x=12.5%	5544	658(7)	3	263(5)	6	10.89(6)	0.02	6.89(7)	0.07	13.49(7)	0.07
$(Mg_{1-x}Fe_x)(Si_{1-x}Fe_x)O_3$	x=12.5%	5713	678(8)	6	266(7)	5	10.89(6)	0.04	6.82(10)	0.07	13.44(8)	0.08
pPv	$MgSiO_3$	5444	655(7)	5	315(5)	9	10.97(6)	0.04	7.61(6)	0.11	14.05(6)	0.11
$(Mg_{1-x}Fe_x)(Si_{1-x}Al_x)O_3$	x=8.3%	5558	665(7)	1	289(6)	11	10.94(6)	0.01	7.21(8)	0.14	13.75(7)	0.11
$(Mg_{1-x}Fe_x)(Si_{1-x}Fe_x)O_3$	x=8.3%	5674	668(7)	2	299(5)	11	10.85(6)	0.02	7.26(6)	0.13	13.71(6)	0.11
$(Mg_{1-x}Fe_x)(Si_{1-x}Al_x)O_3$	x=16.7%	5670	676(7)	1	308(5)	10	10.92(5)	0.01	7.37(6)	0.12	13.84(6)	0.09
$(Mg_{1-x}Fe_x)(Si_{1-x}Fe_x)O_3$	x=16.7%	5902	657(8)	3	268(6)	10	10.55(6)	0.02	6.75(8)	0.14	13.12(7)	0.11

1.7. Averaging schemes

We used the Voigt scheme for estimating the polycrystal bulk and shear moduli K and G from C_{ij}'s, for each mineral. However, it is worth noting that, the difference using the Voigt-

---

[2] $\int_{V_0}^{V_{RT}} d\ln V = \int_0^{300} \frac{\partial \ln V}{\partial T} dT = \int_0^{300} \alpha(T) dT$, assuming $\alpha(T) = AT$ with $\alpha(T = 300\ \mathrm{K}) = 2\times10^{-5}\ \mathrm{K}^{-1}$ (Lin et al., 2014), we get $V_0 = V_{RT}/\exp\left[300\times\frac{\alpha(T=300\ \mathrm{K})}{2}\right] = 0.997V_{RT}$.

Reuss-Hill (VRH) scheme is negligible for Pv; but the difference on G, V_s, and V_p are evident for pPv, as shown in Table S5. We also find that the differences increase with pressure, but are barely dependent on temperature.

2. Benchmarking

We have compared the structure of pure $MgSiO_3$ perovskite (Pv) and post-perovskite (pPv) with previous reports, including both experiments and theory. The calculated compression behavior for Pv and pPv are shown in Fig. S3. Comparing with experiments, the agreement is good for both Pv and pPv. We also fit the pressure-density data to Vinet and to 3rd-order Birch Murnaghan equation of states (EoS), and obtain consistent values for ambient density and bulk modulus for Pv. For pPv, the agreement is fair for lacking of data at low pressures because we are focusing on the high-pressure region that is geophysically interesting.

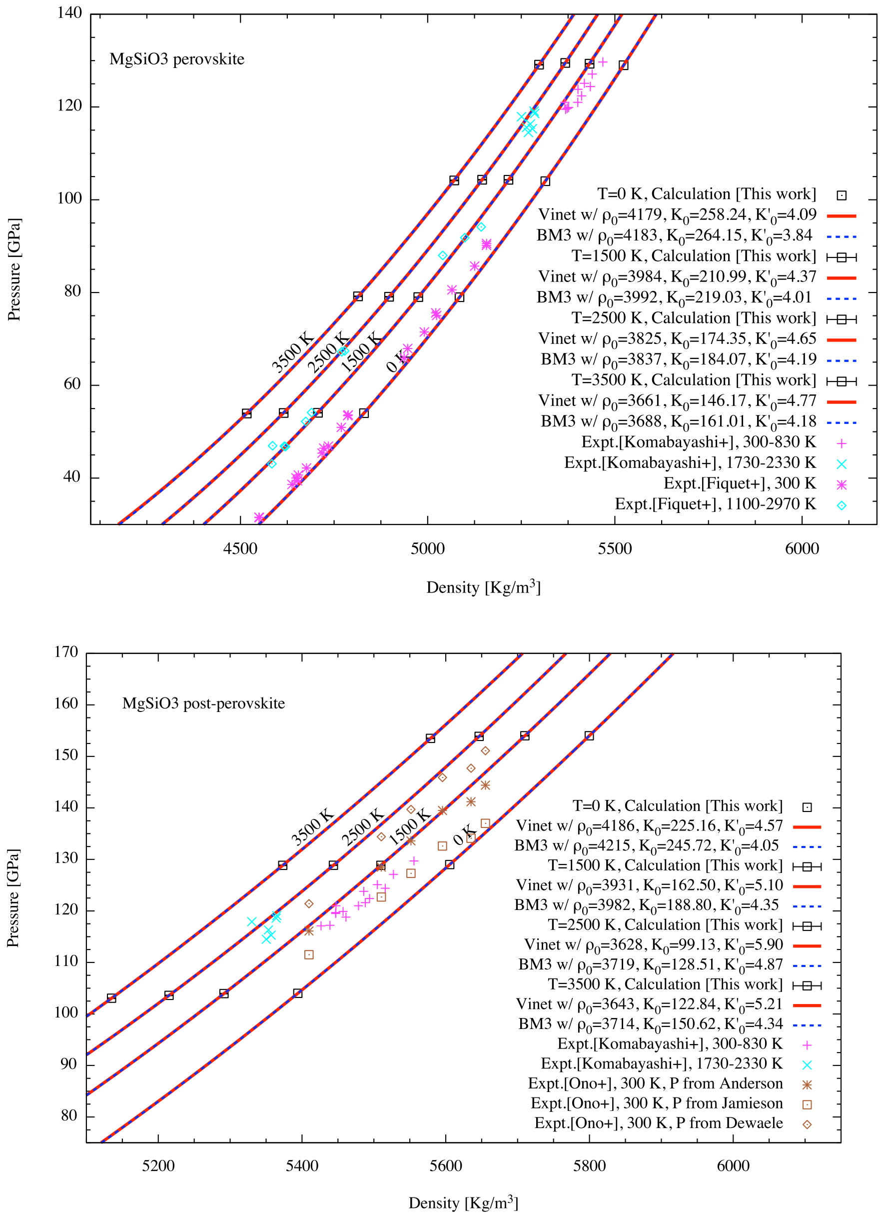

Fig. S3 (color online). The pressure-density relation of Pv and pPv from current calculation (dark squares) and equation-of-state (EoS) fits (red solid line for Vinet, blue dashed line for 3rd-order Birch-Murnaghan) along four different isotherms 0, 1500, 2500, and 3500K, in comparison with experimental measurements. The theoretical pressures have been uniformly uplifted by ΔP=4.0 GPa to account for the deficiency of LDA in underestimating the pressure. The EoS parameters are from fitting the original data (without pressure shift), in order to avoid error accumulation.

In order to gain a better understanding of our calculation results, we look deeper into the structures from our molecular dynamic (MD) simulations in the NPT ensemble by comparing the axial ratio with more previous works. The results for both Pv and pPv have been summarized in Fig. S4. As we can see, the agreement in lattice constants is not always good.

Specifically, the axial ratios at 0 K are higher than that extrapolated from high-temperature simulations by ~0.65% for pPv and a smaller amount for Pv; for pPv, the calculated *b/a* and *c/a* are 0.6% smaller than the experiment by Komabayashi et al. (2008) at high temperature; for Pv, the calculated *b/a* is larger at high temperature by 1% than that from Komabayashi et al. (2008), and *2c/3a* smaller by 0.5% at ambient temperature. On the other hand, our calculation is in good agreement with previous calculations by Zhang et al. (2013) on Pv and Tsuchiya et al. (2004) and Stackhouse et al. (2007) on pPv, as well as some high-T experiments by Tange et al. (2012) on Pv and low-T measurements by Komabayashi et al. (2008). Looking into the discontinuity at 0 K, we found that it is mainly induced by the denser *k* mesh implemented in the static calculations. If using Γ-point only, the axial ratios become smooth functions of temperature. This indicates that the pPv structures that we obtained from Γ-point only MD simulations intrinsically embrace some amount of strain (<1%), which could result in changes in the elastic coefficients and moduli by about 10 GPa. This, however, is of the same order of magnitude as the uncertainty of these quantities from our calculation, and is the best we can do for now, considering the prone-to-instability NPT simulations and general expensiveness of MD calculations.

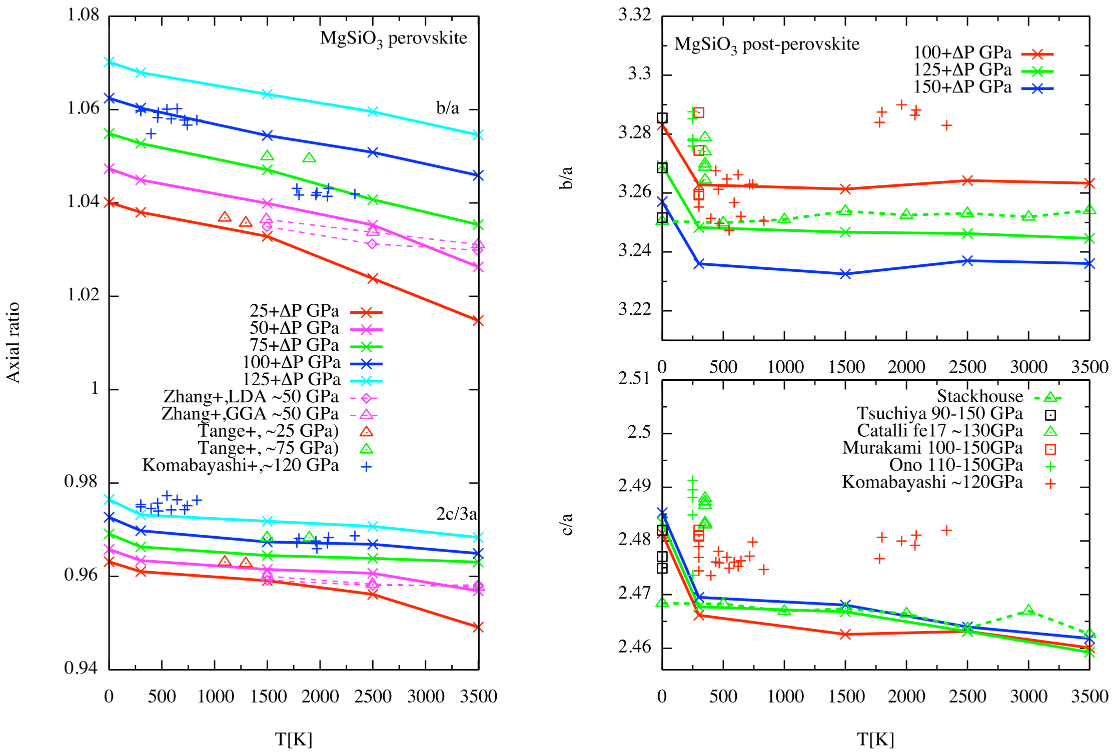

Fig. S4 (color online). The axial ratios of MgSiO3 Pv and pPv as a function of temperature, in comparison to previous theoretical and experimental reports. ΔP denotes the pressure correction on our LDA calculations.

We further benchmark the bulk modulus of iron-bearing MgSiO$_3$. Fig. S5 compares on our calculation with experimental values (from Dorfmann and Duffy, 2014) at two pressures (80 and 125 GPa). Note that both theoretical and experimental data have high (generally over 10 GPa) uncertainty. The overall consistency at 300 K is good, although the confidence level of our results at 300 K is lower than at high temperatures (1500-3500 K), at which the current thermoelasticity study has been carried out. For Fe^{3+}-Fe^{3+} bearing Pv at 80 GPa, the only available experimental data point does not agree with our calculation, future experimental measurements are required to resolve this.

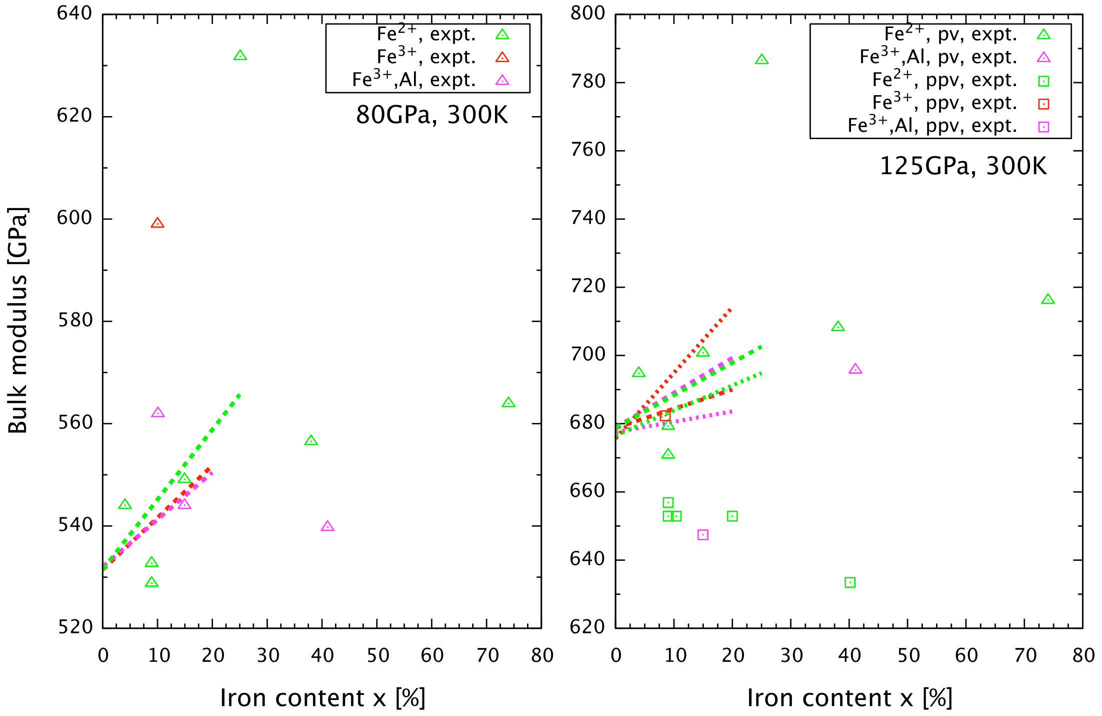

Fig. S5 (color online). The bulk modulus of iron-bearing $MgSiO_3$ Pv and pPv as a function of iron content. Green, red, and pink represent Fe^{2+}, Fe^{3+}-Fe^{3+}, and Fe^{3+}-Al^{3+} bearing systems, respectively. Our data extrapolated to 300 K for Pv (dashed lines) and pPv (dotted lines) are compared with experimental results (shown in the legend, data are from Figs. 2 and 4 in Dorfman and Duffy, 2014). Uncertainties are generally over 10 GPa and are not shown for clarity.

3. Data

Fig. S6 shows the calculated elastic constants as functions of pressure for pure $MgSiO_3$ Pv and pPv. The agreement with a recent calculation on Pv reconfirms the reliability of present calculations. The temperature derivatives of elastic constants of pPv at 125 GPa are summarized in Table S6, comparing with previous studies and that of Pv. The fit parameters (using Eq. (2) in the main context) for C_{ij} are summarized in Table S7. Detailed lists of the density, elasticity, and seismic properties for ferrous iron bearing Pv and pPv can be found in the Table S8; the data for ferric iron bearing Pv and pPv are listed in the file Ferric_iron_bearing_MgSiO3.csv.

The shear wave anisotropy of pure and Fe/Al-bearing Pv and pPv as functions of pressure and temperature are summarized in Figs. S7-8. The transverse isotropy $\xi = V_{SH}^2/V_{SV}^2$ for different Pv and pPv phases as functions of pressure is shown in Fig. S9. The transverse isotropy of single-crystal and textured pPv phases are compared as functions of pressure in Fig. S10.

4. Discussion on Variations in the D″

For variations in velocity and density in the lowermost mantle, the reader is referred to, e.g., Lekic et al. (2012), Ishii and Tromp (1999), Simmons et al. (2010). This could reflect significant thermal and compositional variations (e.g. Trampert et al., 2004).

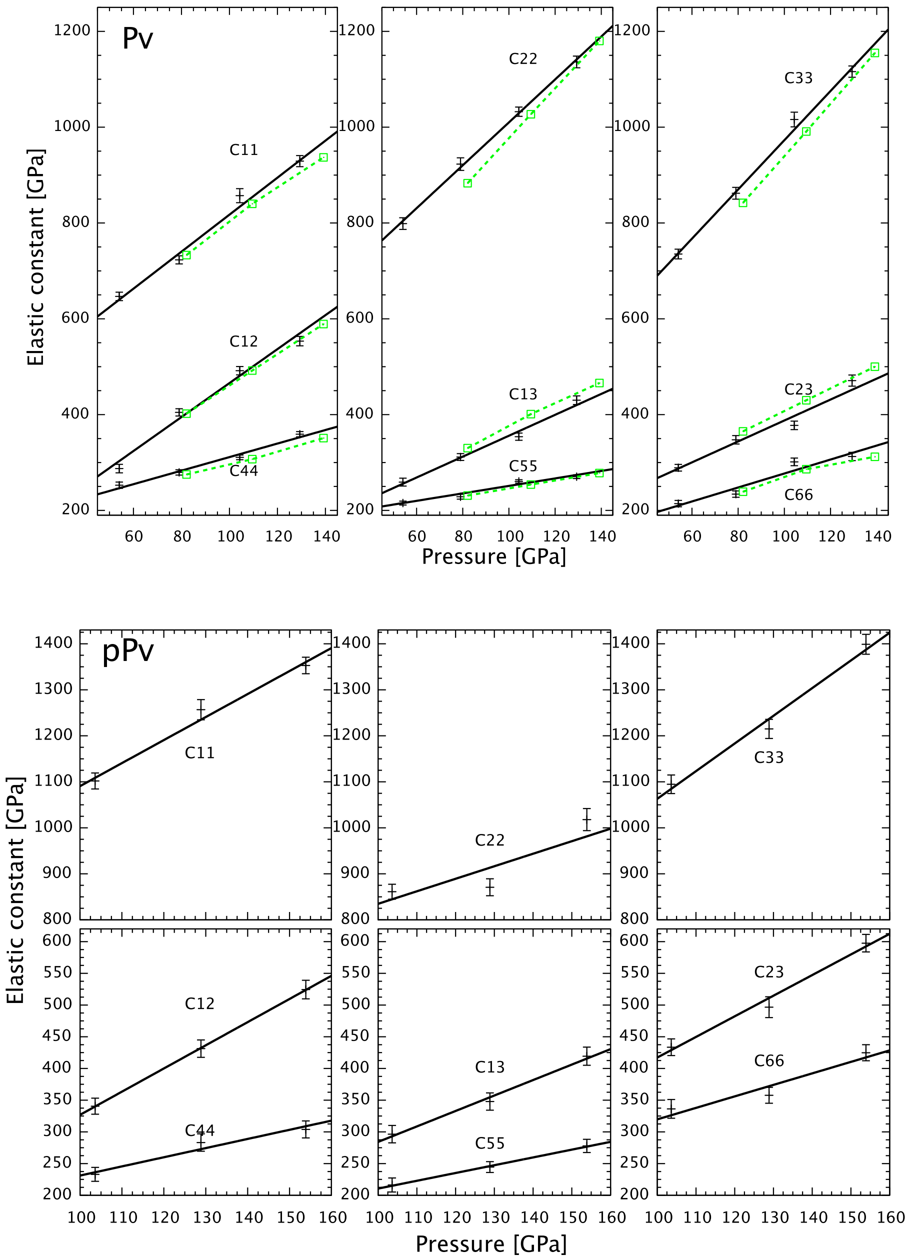

Fig. S6 The pressure dependence of elastic constants of pure $MgSiO_3$ Pv (top) and pPv (pPv) at 2500 K. Previous calculations by Zhang et al. (2013) are shown in green dashed line points for comparison. A pressure correction of 4.0 GPa and 1.9 GPa has been applied to ours and Zhang et al.'s data, respectively.

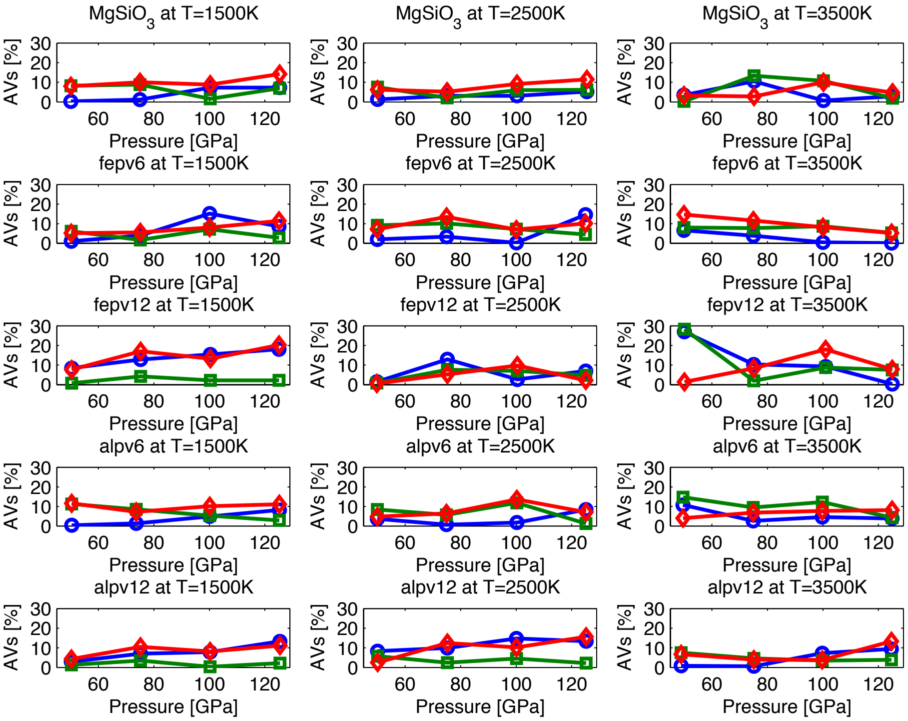

MgSiO$_3$ at T=1500K
MgSiO$_3$ at T=2500K
MgSiO$_3$ at T=3500K
fepv6 at T=1500K
fepv6 at T=2500K
fepv6 at T=3500K
fepv12 at T=1500K
fepv12 at T=2500K
fepv12 at T=3500K
alpv6 at T=1500K
alpv6 at T=2500K
alpv6 at T=3500K
alpv12 at T=1500K
alpv12 at T=2500K
alpv12 at T=3500K

Fig. S7 (color online). The shear anisotropy of pure and Fe/Al-bearing Pv as a function of pressure along three isotherms relevant to the Earth's lower mantle temperature. Blue, green, and red lines correspond to shear waves propagating along the [100], [010], and [001] direction, respectively.

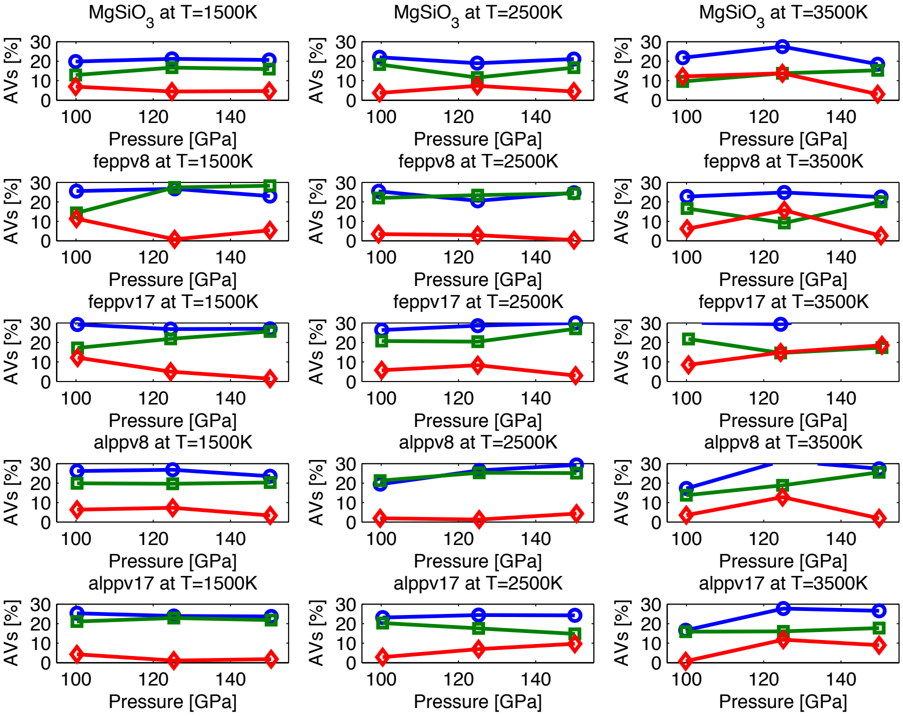

MgSiO$_3$ at T=1500K
MgSiO$_3$ at T=2500K
MgSiO$_3$ at T=3500K
feppv8 at T=1500K
feppv8 at T=2500K
feppv8 at T=3500K
feppv17 at T=1500K
feppv17 at T=2500K
feppv17 at T=3500K
alppv8 at T=1500K
alppv8 at T=2500K
alppv8 at T=3500K
alppv17 at T=1500K
alppv17 at T=2500K
alppv17 at T=3500K

Fig. S8 (color online). The shear anisotropy of pure and Fe/Al-bearing pPv as a function of pressure along three isotherms relevant to the Earth's lower mantle temperature. Blue, green, and red lines correspond to shear waves propagating along the [100], [010], and [001] direction, respectively.

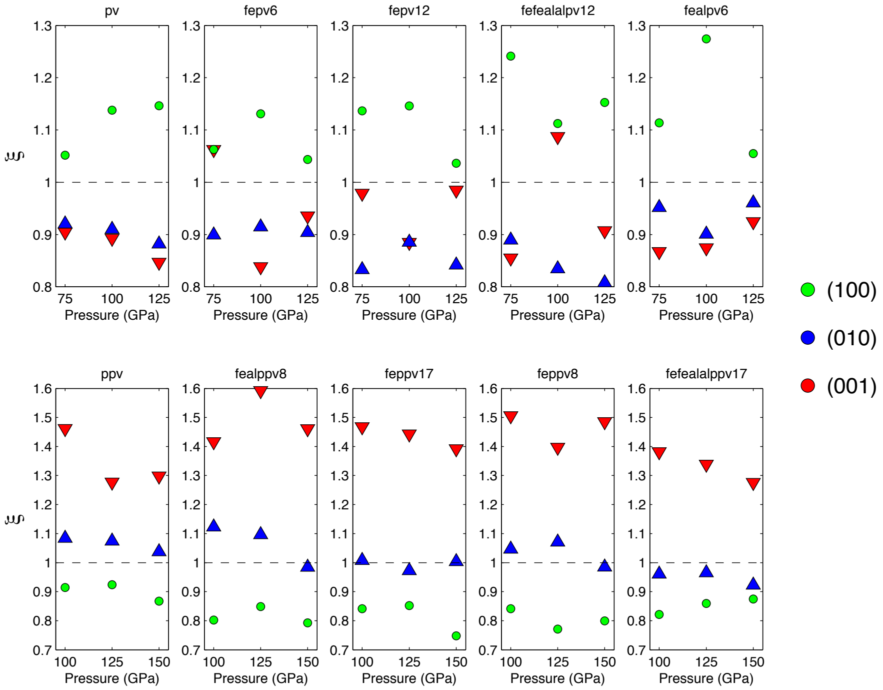

Fig. S9 (color online). The transverse isotropy for different single-crystal Pv and pPv phases at *T*=2500K. The errorbar is about 0.1. Red down triangles, blue up triangles, and green spheres denote split planes (001), (010), and (100), respectively.

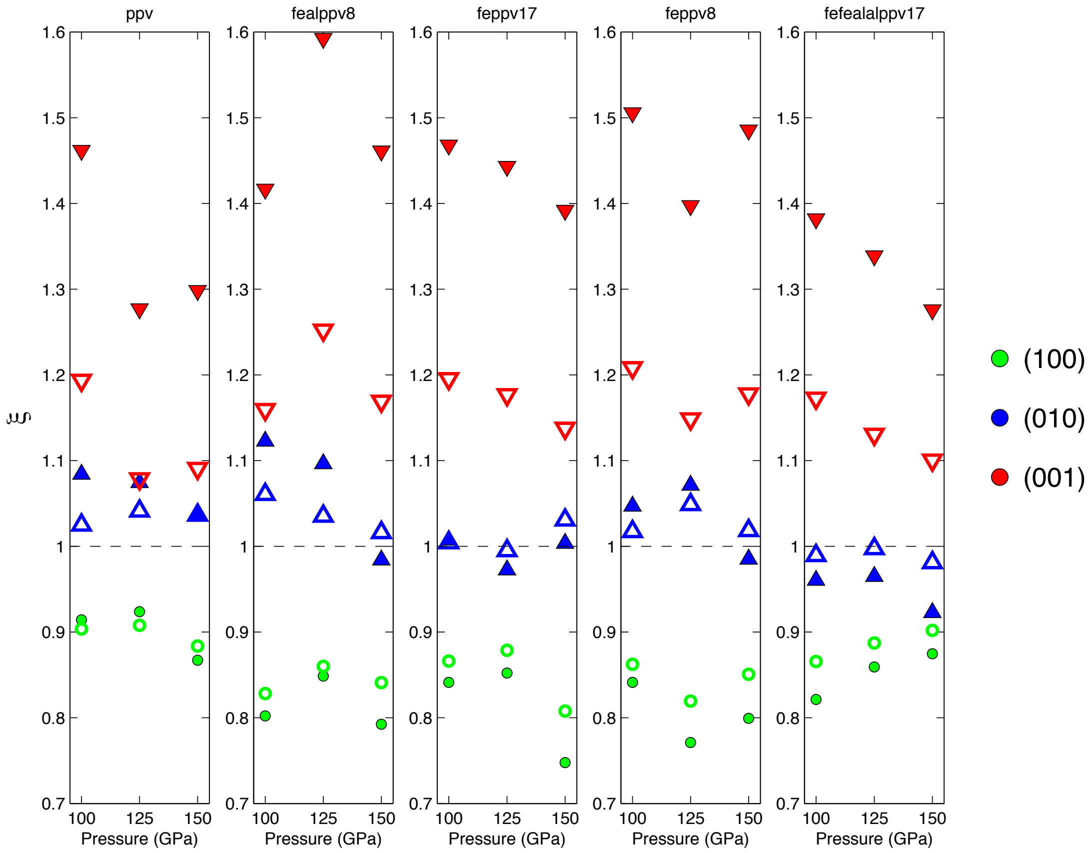

Fig. S10 (color online). The transverse isotropy for single-crystal (filled symbol) and textured (open symbol) pPv phases at *T*=2500K. Red down and blue up triangles, and green spheres denote (001), (010), and (100) split planes, respectively.

Table S6

Temperature derivative of adiabatic elastic constants (in units of GPa/K) of pure and Fe/Al-bearing pPv and Pv at 125 GPa. The numbers in parenthesis are the uncertainties on the last digit of the value. SB07 and RW06 denote previous calculations by Stackhouse and Brodholt (2007) and Wentzcovitch, et al. (2006), respectively.

Name		dC11/dT	dC22/dT	dC33/dT	dC12/dT	dC13/dT	dC23/dT	dC44/dT	dC55/dT	dC66/dT
pPv	MgSiO3	-0.037(13)	-0.039(15)	-0.038(14)	0.009(9)	-0.018(9)	-0.013(8)	-0.005(8)	-0.024(6)	-0.025(9)
$(Mg_{1-x}Fe_x)(Si_{1-x}Fe_x)O_3$	x=8.3%	-0.045(16)	-0.033(14)	-0.067(15)	-0.005(10)	0.010(10)	-0.006(10)	0.015(13)	-0.011(7)	-0.042(10)
	x=16.7%	-0.052(18)	-0.039(12)	-0.067(13)	-0.030(10)	-0.011(10)	-0.014(10)	-0.003(14)	-0.027(6)	-0.037(9)
$(Mg_{1-x}Fe_x)(Si_{1-x}Al_x)O_3$	x=8.3%	-0.027(12)	-0.009(16)	-0.056(15)	0.012(9)	0.012(10)	-0.011(11)	-0.013(10)	-0.026(9)	-0.038(11)
	x=16.7%	-0.034(14)	-0.036(15)	-0.046(13)	-0.006(8)	-0.009(9)	-0.021(8)	0.009(9)	-0.027(6)	-0.026(10)
$MgSiO_3$, pPv	SB07	-0.046	-0.024	-0.046	-0.005	-0.003	-0.003	-0.012	-0.014	-0.029
$MgSiO_3$, pPv	RW06	-0.083	-0.037	-0.069	0.001	0.022	-0.005	-0.011	-0.028	-0.045
Pv	MgSiO3	-0.039(11)	-0.040(11)	-0.029(11)	-0.008(9)	-0.006(9)	0.007(9)	-0.025(6)	0.003(4)	-0.009(9)
(Mg1-xFex)(Si1-xFex)O3	x=6.25%	-0.024(17)	-0.068(14)	-0.049(15)	0.001(10)	-0.003(10)	0.002(10)	-0.020(8)	0.000(6)	-0.017(9)
	x=12.5%	-0.035(17)	-0.065(20)	-0.020(17)	0.003(12)	-0.013(12)	0.010(12)	-0.026(12)	0.012(9)	-0.036(12)

(Mg1-xFex)(Si1-xAlx)O3	x=6.25%	-0.029(12)	-0.057(15)	-0.050(14)	-0.004(9)	-0.010(9)	-0.005(10)	-0.035(6)	-0.019(5)	-0.033(9)
	x=12.5%	-0.060(11)	-0.053(13)	-0.035(13)	0.006(8)	-0.006(9)	-0.006(10)	-0.013(7)	-0.018(6)	-0.032(9)

Table S7

Fitting parameters (corresponding to Eq. (2) in the main text) for the elastic constants of Fe/Al-bearing Pv and pPv. k and b are in units of 1/K, GPa/K, 1, and GPa for A_0, A_1, A_2, and A_3, respectively.

Name	A0-k	A0-b	A1-k	A1-b	A2-k	A2-b	A3-k	A3-b
(Mg$_{1-x}$Fe$_x$)(Si$_{1-x}$Fe$_x$)O$_3$ Pv								
C11	5.44E-03	-2.12E-04	-5.39E-01	-1.25E-02	1.86E-02	6.27E+00	4.28E-01	5.64E+02
C12	3.77E-03	-1.25E-04	-3.76E-01	9.70E-03	1.41E-02	4.72E+00	3.42E-01	4.26E+02
C44	-1.90E-03	1.06E-04	1.08E-01	-2.75E-02	1.04E-02	3.90E+00	2.37E-01	3.57E+02
C22	-5.40E-03	5.23E-04	3.96E-01	-9.40E-02	1.78E-02	6.72E+00	4.39E-01	6.20E+02
C13	1.01E-03	-9.98E-05	-1.78E-01	1.25E-02	1.40E-02	4.50E+00	3.25E-01	4.08E+02
C55	-9.69E-04	2.04E-04	1.50E-01	-2.56E-02	7.73E-03	2.78E+00	1.69E-01	2.45E+02
C33	5.82E-03	8.35E-05	-5.36E-01	-5.95E-02	1.87E-02	6.16E+00	4.33E-01	5.84E+02
C23	-2.02E-03	2.76E-04	1.72E-01	-2.06E-02	1.35E-02	4.69E+00	3.35E-01	4.21E+02
C66	1.32E-03	-1.16E-05	-2.15E-01	-1.85E-02	1.29E-02	4.25E+00	3.02E-01	3.71E+02
(Mg$_{1-x}$Fe$_x$)(Si$_{1-x}$Al$_x$)O$_3$ Pv								
C11	9.76E-04	-1.92E-04	-2.44E-01	-1.31E-02	1.83E-02	5.57E+00	4.21E-01	5.26E+02
C12	3.77E-03	-3.09E-05	-4.08E-01	-5.51E-03	1.39E-02	4.22E+00	3.37E-01	3.95E+02
C44	1.43E-03	2.34E-05	-1.98E-01	-2.33E-02	1.02E-02	3.47E+00	2.33E-01	3.32E+02
C22	-3.59E-03	4.34E-04	1.37E-01	-8.49E-02	1.75E-02	5.58E+00	4.28E-01	5.17E+02
C13	1.84E-03	-2.07E-04	-1.68E-01	2.28E-02	1.38E-02	4.01E+00	3.21E-01	3.72E+02
C55	-1.88E-03	1.52E-04	7.30E-02	-2.09E-02	7.60E-03	2.48E+00	1.65E-01	2.42E+02
C33	3.01E-03	1.41E-04	-3.74E-01	-6.29E-02	1.87E-02	5.61E+00	4.33E-01	5.24E+02
C23	-3.81E-03	2.81E-04	3.18E-01	-1.82E-02	1.35E-02	4.35E+00	3.34E-01	3.85E+02
C66	-7.65E-04	-5.80E-05	2.04E-02	-1.57E-02	1.27E-02	3.99E+00	2.98E-01	3.59E+02
(Mg$_{1-x}$Fe$_x$)(Si$_{1-x}$Fe$_x$)O$_3$ pPv								
C11	9.31E-03	-7.98E-04	-1.28E+00	7.05E-02	4.35E-02	8.69E+00	7.61E-01	1.08E+03
C12	-4.70E-03	2.67E-04	4.16E-01	-2.33E-02	3.29E-02	6.44E+00	5.73E-01	8.11E+02
C44	4.34E-03	-3.71E-05	-5.63E-01	-7.15E-03	2.78E-02	7.24E+00	4.95E-01	9.03E+02
C22	-4.70E-03	5.31E-04	5.06E-01	-9.89E-02	4.30E-02	7.34E+00	7.76E-01	9.09E+02
C13	5.05E-03	-6.66E-04	-6.16E-01	7.50E-02	3.12E-02	6.02E+00	5.46E-01	7.50E+02
C55	-4.16E-03	2.23E-04	4.94E-01	-4.51E-02	2.21E-02	3.90E+00	3.59E-01	4.87E+02
C33	-4.64E-03	3.79E-04	3.43E-01	-7.71E-02	4.40E-02	7.05E+00	7.16E-01	8.94E+02
C23	-5.86E-03	6.41E-04	6.95E-01	-8.29E-02	3.28E-02	5.61E+00	5.68E-01	6.90E+02
C66	-1.47E-03	-6.14E-05	8.75E-02	-1.70E-02	2.99E-02	5.27E+00	4.96E-01	6.74E+02
(Mg$_{1-x}$Fe$_x$)(Si$_{1-x}$Al$_x$)O$_3$ pPv								
C11	3.70E-03	-6.37E-04	-5.92E-01	5.05E-02	4.22E-02	7.12E+00	7.41E-01	9.10E+02
C12	-5.42E-03	4.62E-04	6.28E-01	-5.18E-02	3.13E-02	5.31E+00	5.51E-01	6.59E+02
C44	3.72E-04	-1.39E-04	-1.23E-02	1.60E-03	2.67E-02	4.65E+00	4.79E-01	5.89E+02

C22	-3.69E-03	4.45E-04	4.03E-01	-8.90E-02	4.18E-02	7.98E+00	7.48E-01	1.00E+03
C13	8.26E-03	-7.81E-04	-8.94E-01	8.64E-02	3.01E-02	4.90E+00	5.30E-01	6.25E+02
C55	-8.33E-04	6.38E-05	1.01E-01	-2.46E-02	2.22E-02	3.94E+00	3.60E-01	5.09E+02
C33	-2.40E-03	8.96E-04	1.79E-01	-1.46E-01	4.34E-02	7.64E+00	7.06E-01	9.64E+02
C23	-2.12E-03	4.01E-04	2.99E-01	-4.93E-02	3.25E-02	5.97E+00	5.68E-01	7.41E+02
C66	2.80E-03	-9.25E-06	-4.08E-01	-2.23E-02	2.95E-02	5.28E+00	4.95E-01	6.73E+02

Table S8

Density and adiabatic elastic and seismic properties for Fe^{2+} bearing Pv and pPv at different P, T conditions. The values in parenthesis denote the error.

T[K]	2000	4000	2000	4000
P[GPa]	100	100	136	136
$(Mg_{0.75}Fe_{0.25})SiO_3$ Pv				
ρ [kg/m^3]	5532	5375	5857	5717
C11[GPa]	822.44(5.24)	720.84(10.79)	940.29(9.03)	894.72(13.27)
C22[GPa]	980.51(9.62)	849.01(15.85)	1151.59(7.65)	1020.73(14.10)
C33[GPa]	941.25(9.94)	827.20(23.95)	1137.57(8.82)	1039.02(20.41)
C12[GPa]	485.55(6.59)	451.07(13.69)	608.64(5.95)	618.63(10.31)
C13[GPa]	399.96(7.71)	411.66(15.42)	489.99(6.78)	475.96(16.25)
C23[GPa]	438.51(7.20)	425.31(11.32)	532.45(8.07)	531.07(9.76)
C44[GPa]	291.27(3.62)	241.62(0.69)	327.59(3.34)	280.81(9.62)
C55[GPa]	236.50(4.30)	213.65(3.93)	258.31(2.17)	241.40(5.85)
C66[GPa]	241.19(8.20)	218.16(14.42)	307.84(9.06)	245.27(11.85)
K^S[GPa]	599.14(3.22)	552.57(6.24)	721.29(3.15)	689.53(5.72)
G[GPa]	248.47(2.37)	208.62(3.95)	285.31(2.35)	242.08(4.03)
V_b[km/s]	10.41(0.03)	10.14(0.06)	11.10(0.02)	10.98(0.05)
V_s[km/s]	6.70(0.03)	6.23(0.06)	6.98(0.03)	6.51(0.05)
V_p[km/s]	12.97(0.03)	12.43(0.06)	13.71(0.03)	13.31(0.05)
$(Mg_{0.75}Fe_{0.25})SiO_3$ pPv				
ρ [kg/m^3]	5614	5454	5945	5800
C11[GPa]	1071.27(4.81)	999.04(16.22)	1250.32(8.97)	1166.04(12.87)
C22[GPa]	820.66(4.40)	765.46(11.81)	973.85(5.40)	874.94(12.25)
C33[GPa]	1055.93(7.48)	946.37(13.96)	1276.18(11.76)	1135.09(20.23)
C12[GPa]	398.56(6.17)	413.88(18.63)	529.23(7.49)	515.19(16.74)
C13[GPa]	344.47(7.04)	339.45(17.38)	407.95(11.61)	417.84(14.29)
C23[GPa]	443.23(6.29)	431.01(10.83)	550.59(5.01)	541.41(11.94)
C44[GPa]	218.69(5.21)	197.70(18.36)	266.10(6.82)	238.97(9.00)
C55[GPa]	212.15(3.64	180.59(7.17	249.92(3.38	212.20(5.61
C66[GPa]	300.23(6.68)	276.82(11.35)	388.37(5.87)	325.26(9.51)
K^S[GPa]	591.15(2.74)	564.39(6.72)	719.54(3.70)	680.55(6.32)
G[GPa]	263.65(2.10)	232.79(5.17)	315.05(2.40)	268.73(3.76)

V_b[km/s]	10.26(0.02)	10.17(0.06)	11.00(0.03)	10.83(0.05)
V_s[km/s]	6.85(0.03)	6.53(0.07)	7.28(0.03)	6.81(0.05)
V_p[km/s]	12.96(0.03)	12.66(0.07)	13.85(0.03)	13.38(0.05)

References

Caracas, R., 2010. Spin and structural transitions in AlFeO3 and FeAlO3 perovskite and post-perovskite. Phys. Earth Planet. Inter. 182 (1-2), 10–17. doi:10.1016/j.pepi.2010.06.001

Catalli, K., Shim, S.-H., Dera, P., Prakapenka, V.B., Zhao, J., Sturhahn, W., Chow, P., Xiao, Y., Cynn, H., Evans, W.J., 2011. Effects of the Fe3+ spin transition on the properties of aluminous perovskite—New insights for lower-mantle seismic heterogeneities. Earth Planet. Sci. Lett. 310 (3-4), 293–302. doi:10.1016/j.epsl.2011.08.018

Dorfman, S.M., Duffy, T.S., 2014. Effect of Fe-enrichment on seismic properties of perovskite and post-perovskite in the deep lower mantle. Geophys. J. Int. 197 (2), 910–919.

Fiquet, G., Dewaele, A., Andrault, D., Kunz, M., 2000. Thermoelastic properties and crystal structure of MgSiO perovskite at lower mantle pressure and temperature conditions. Geophys, Res. Lett. 27 (1), 21–24.

Ishii, M., Tromp, J., 1999. Normal-mode and free-air gravity constraints on lateral variations in velocity and density of Earth's mantle. Science 285, 1231–1236, doi:10.1126/science.285.5431.1231.

Lekic, V., Cottaar, S., Dziewonski, A.M., Romanowicz, B., 2012. Cluster analysis of global lower mantle tomography: A new class of structure and implications for chemical heterogeneity. Earth Planet. Sci. Lett. 357-358, 68–77, doi:10.1016/j.epsl.2012.09.014.

Monkhorst, H.J., Pack, J.D., 1976. Special points for Brillouin-zone integrations. Phys. Rev. B 13, 5188. http://dx.doi.org/10.1103/PhysRevB.13.5188

Komabayashi, T., Hirose, K., Sugimura, E., Sata, N., Ohishi, Y., Dubrovinsky, L.S., 2008. Simultaneous volume measurements of post-perovskite and perovskite in MgSiO3 and their thermal equations of state. Earth Planet. Sci. Lett. 265 (3-4), 515–524. doi:10.1016/j.epsl.2007.10.036

Lin, Y., Cohen, R.E., Stackhouse, S., Driver, K.P., Militzer, B., Shulenburger, L., Kim, J., 2014. Equations of state and stability of $MgSiO_3$ perovskite and post-perovskite phases from quantum Monte Carlo simulations. Phys. Rev. B 90 (18), 184103. doi:10.1103/PhysRevB.90.184103

Shieh, S.R., Duffy, T.S., Kubo, A., Shen, G., Prakapenka, V. B., Sata, N., Hirose, K., Ohishi, Y., 2005. Equation of state of the postperovskite phase synthesized from a natural (Mg,Fe)SiO3 orthopyroxene. Proc. Natl. Acad. Sci. USA 103 (9), 3039–3043.

Simmons, N., Forte, A., Boschi, L., Grand, S., 2010. GyPSuM: A joint tomographic model of mantle density and seismic wave speeds. J. Geophys. Res. 115, B12310, doi:10.1029/2010JB007631.

Trampert, J., Deschamps, F., Resovsky, J., Yuen, D., 2004. Probabilistic tomography maps chemical heterogeneities throughout the lower mantle. Science 306 (5697), 853–856. doi:10.1126/science.1101996

Tsuchiya, T., Wentzcovitch, R., da Silva, C., de Gironcoli, S., 2006. Spin Transition in Magnesiowüstite in Earth’s Lower Mantle. Phys. Rev. Lett. 96(19), 198501. doi:10.1103/PhysRevLett.96.198501